SANDIA REPORT

SAND2018-13260 Unlimited Release
Printed

Ductile Fracture - Gradient Regularization

Andrew J. Stershic, Brandon L. Talamini, Jakob T. Ostien

Prepared by
Sandia National Laboratories
Albuquerque, New Mexico 87185 and Livermore, California 94550

Sandia National Laboratories is a multimission laboratory managed and operated by National Technology and Engineering Solutions of Sandia, LLC, a wholly owned subsidiary of Honeywell International, Inc., for the U.S. Department of Energy's National Nuclear Security Administration under contract DE-NA0003525.

Sandia National Laboratories

Issued by Sandia National Laboratories, operated for the United States Department of Energy by National Technology and Engineering Solutions of Sandia, LLC.

Available to DOE and DOE contractors from
U.S. Department of Energy
Office of Scientific and Technical Information
P.O. Box 62
Oak Ridge, TN 37831

Telephone: (865) 576-8401
Facsimile: (865) 576-5728
E-Mail: reports@adonis.osti.gov
Online ordering: http://www.osti.gov/bridge

Available to the public from
U.S. Department of Commerce
National Technical Information Service
5285 Port Royal Rd
Springfield, VA 22161

Telephone: (800) 553-6847
Facsimile: (703) 605-6900
E-Mail: orders@ntis.fedworld.gov
Online ordering: http://www.ntis.gov/help/ordermethods.asp?loc=7-4-0#online

SAND2018-13260 Unlimited Release
Printed

Ductile Fracture - Gradient Regularization

Andrew J. Stershic
Multi-Physics Modeling & Simulation (8259)
Sandia National Laboratories
Livermore, CA

Brandon L. Talamini
Mechanics of Materials (8343)
Sandia National Laboratories
Livermore, CA

Jakob T. Ostien
Mechanics of Materials (8343)
Sandia National Laboratories
Livermore, CA

Abstract

Nuclear weapons alteration (ALT) and life extension programs (LEP) are of primary interest to the mission of Sandia National Laboratories. These programs continue to require experimental exploration and computational simulation of ductile failure scenarios to address qualification. Therefore, we invest in generating understanding about ductile failure as demonstrated though experimental procedures and computational simulation of engineering environments. In particular, we study an approach to ductile failure that incorporates the notion of phase-field fracture into our models of inelasticity appropriate for structural alloys. This report covers the formulations of the constitutive model and fracture models used within the phase-field approach and provides some numerical examples highlighting features and the state of the capability.

Contents

List of Figures

List of Tables

Chapter 1

Introduction

Nuclear weapons alteration (ALT) and life extension programs (LEP) are of primary interest to the mission of Sandia National Laboratories. These programs continue to require experimental exploration and computational simulation of ductile failure scenarios to address qualification. Many weapons system mechanical analyses probe the margins of component or system failure, drawing upon expertise and understanding in the ductile behavior of structural alloys up to and including failure. This expertise and understanding is demonstrated through experimental exploration, as well as through the development and usage of modeling and simulation. Accurate ductile failure modeling requires several capabilities to robustly work together, including the finite element solver, ductile constitutive model and failure model, regularization method, and potentially a surface creation method. The purpose of this report is the exploration of a ductile failure theory based on the phase-field fracture school of thought.

The phase-field model for fracture is distinguished by its clear derivation from an energy functional wherein the surficial energy of Griffith fracture is replaced by a volumetric term that represents a crack diffusively. The corresponding Euler-Lagrange equations define a continuum damage model in which the damage field has a finite length scale. Consequently, the phase-field model is solved by evolving damage to minimize the energy functional [6, 4]. As a continuum damage model, the phase-field approach can intrinsically represent arbitrary crack nucleation, growth, branching, and coalescence without the need for front-tracking or extension algorithms [12]. From this perspective, the phase-field approach presents as a scion of the gradient-damage class of models [19, 11].

The advantages of the phase-field fracture model, in particular its simplicity of implementation, have drawn much attention in the scientific community, and the model has become more widespread in application. The first generation of phase-field models was primarily applied to brittle and quasi-brittle materials, in which the material response is elastic until failure [5, 8]. From this application, two formulations have emerged as dominant: the classical model and threshold model. The classical model uses a quadratic damage potential in the fracture energy definition and tends to damage more diffusively though the domain, damaging minutely even from low stresses. In contrast, the threshold model uses a linear damage potential and diffuses damage in a region more proximate to a crack, evolving dam-

age only once a given stress- or energy-based threshold is reached [2].

Some researchers have sought means to link gradient-damage and phase-field models to cohesive models through particular choices of the damage degradation function and the volumetric fracture energy definition [13, 23, 22]. By adding a second length scale, these approaches alleviate the paradox of having the regularization length be interpreted as a physical length scale by some and as a numerical parameter by others. More recently, researchers have explored the application of a phase-field fracture model to ductile failure problems through the consideration of plastic strain and plastic work as contributing factors to damage growth [2, 3, 16, 1].

In this study, our objective is to formulate and implement a phase-field model for ductile failure into Sandia National Laboratories' primary finite element code for solid mechanics, *Sierra/SM*. In Chapter 2, the theoretical framework for a hyperelastic plasticity model and phase-field model are provided. Implementational details are discussed in Chapter 3. Demonstrations of the phase-field model and model verification efforts are presented in Chapter 4. Lastly, Chapter 5 provides a summary of our work and an outlook for the future.

Chapter 2

Theory

The primary effort of this study is the implementation of a phase-field fracture model that is appropriate for application to ductile materials. The theoretical framework of this model is described in this chapter, while the implementation is discussed in Chapter 3. First, the governing equations and constitutive framework are presented, then the details of the hyperelastic plasticity model *FeFp* and the phase-field fracture model. Together these are implemented in *Sierra/SM* as *PhaseFieldFeFp*, a hyperelastic ductile plasticity model with phase-field failure representation.

Kinematics

We consider a solid body that is deforming (and possibly fracturing) under the action of external loads. We assume isothermal conditions. Let $\boldsymbol{\chi}(\boldsymbol{X}, t)$ be the deformation map at time t from the material point $\boldsymbol{X}$ in the reference configuration $B_0 \subset \mathbb{R}^3$ to the spatial point $\boldsymbol{x}$ in the current configuration $B_t \subset \mathbb{R}^3$. We denote the deformation gradient by $\boldsymbol{F} = \boldsymbol{\nabla}\boldsymbol{\chi}$, where here and in the following the operator $\boldsymbol{\nabla}$ indicates differentiation with respect to $\boldsymbol{X}$.

Plastic deformation is modeled through the framework of the multiplicative decomposition

$$\boldsymbol{F} = \boldsymbol{F}^e \boldsymbol{F}^p.$$

We refer to $\boldsymbol{F}^e$ and $\boldsymbol{F}^p$ as the elastic and plastic distortions. The plastic distortion $\boldsymbol{F}^p$ evolves according to the flow rule[1]

$$\dot{\boldsymbol{F}}^p \boldsymbol{F}^{p-1} = \dot{\bar{\varepsilon}}^p \boldsymbol{N}^p, \tag{2.1}$$

wherein $\dot{\bar{\varepsilon}}^p$ specifies the magnitude of plastic flow, and $\boldsymbol{N}^p$ the flow direction. The tensor $\boldsymbol{N}^p$ is subject to the constraints

$$\operatorname{tr} \boldsymbol{N}^p = \boldsymbol{0}, \qquad \boldsymbol{N}^p : \boldsymbol{N}^p = \frac{3}{2} \tag{2.2}$$

[1]We use Newton's overdot notation to signify the material time derivative, i.e., the time derivative taken holding $\boldsymbol{X}$ fixed.

which ensure that plastic flow is isochoric, as is commonly assumed for metal plasticity, and that the scale of $\boldsymbol{N}^p$ is such that $\dot{\bar{\varepsilon}}^p$ can be interpreted as the *uniaxial* equivalent plastic strain rate. Plastic deformation is assumed irreversible, thus the unilateral constraint

$$\dot{\bar{\varepsilon}}^p \geq 0 \tag{2.3}$$

is imposed.

Fracture is modeled in a diffuse manner with a macroscopic scalar damage field

$$\phi(\boldsymbol{X}, t), \qquad 0 \leq \phi \leq 1, \tag{2.4}$$

where a value of zero signifies virgin material, and a value of one indicates that the material point has lost all capacity to carry load. We refer to this field interchangeably as the *phase* or the *damage*. Damage is regarded as an irreversible process, thus the phase field evolution is subject to the constraint

$$\dot{\phi} \geq 0. \tag{2.5}$$

In some of the considered models, the driving force for the phase field diminishes as $\phi \to 1$, and the upper bound need not be imposed as a constraint. In models where this is not the case, we additionally require

$$\dot{\phi} = 0 \quad \text{if } \phi = 1 \tag{2.6}$$

The local thermodynamic state at time t of any material point $\boldsymbol{X}$ is taken to be fully specified by the set of variables

$$\mathcal{U} = \{\boldsymbol{\chi}(\boldsymbol{X}, t), \phi(\boldsymbol{X}, t), \bar{\varepsilon}^p(\boldsymbol{X}, t), \boldsymbol{F}^p(\boldsymbol{X}, t)\},$$

We use the notation

$$\mathcal{V} = \{\dot{\boldsymbol{\chi}}, \dot{\phi}, \dot{\bar{\varepsilon}}^p, \dot{\boldsymbol{F}}^p\}$$

to refer to the set of generalized velocities, which constitute the set of primary unknowns for the problem. Due to the flow rule (2.1), $\dot{\boldsymbol{F}}^p$ may also be replaced with $\boldsymbol{N}^p$ as a primary unknown.

The deformation and phase fields are subject to Dirichlet boundary conditions

$$\begin{aligned} \boldsymbol{\chi} &= \bar{\boldsymbol{\chi}}, \quad \text{on } \partial_{\boldsymbol{\chi}} B_0, \\ \phi &= \bar{\phi}, \quad \text{on } \partial_{\phi} B_0, \end{aligned} \tag{2.7}$$

where $\partial_{\boldsymbol{\chi}} B_0 \subseteq \partial B_0$, and $\partial_{\phi} \subseteq \partial B_0$. For quasi-static problems, $\partial_{\boldsymbol{\chi}} B_0$ must be non-empty for the problem to be well posed.

Governing equations

Our goal in this section is to write the balance laws of the system in weak form, which can then be used as the basis for discretization with finite elements. Phase-field methods for

fracture in brittle elastic solids are firmly established; we cite a few representative examples [6, 4, 5, 8]. The theoretical framework for brittle fracture enjoys a variational structure, and in particular derives from a minimization principle. This is a great advantage, both in theory and practice, as it allows use of powerful tools from mathematical optimization. We shall seek to preserve a variational structure for phase-field fracture with dissipative material behavior.

The weak form of the problem is constructed though the principle of virtual power. The expenditure of power in the body is assumed to depend on $\mathcal{V}$ through the fields

$$\dot{\Lambda} = \left\{ \dot{\boldsymbol{F}}, \dot{\boldsymbol{F}}^p, \dot{\tilde{\varepsilon}}^p, \dot{\phi}, \boldsymbol{\nabla}\dot{\phi} \right\}, \tag{2.8}$$

which we collectively refer to as the set $\dot{\Lambda}$ for notational convenience. The power expenditure assumption over any part $P \subseteq B_0$ takes the mathematical form

$$\mathcal{P}_{\text{int}}(\mathcal{V}) = \int_P \left(\boldsymbol{P} : \boldsymbol{\nabla}\dot{\boldsymbol{\chi}} + \boldsymbol{\Sigma}^p : \dot{\boldsymbol{F}}^p + Y\dot{\tilde{\varepsilon}}^p + f\dot{\phi} + \boldsymbol{\xi} \cdot \boldsymbol{\nabla}\dot{\phi} \right) \mathrm{d}V \,, \tag{2.9}$$

in which

$$\mathcal{F} = \{ \boldsymbol{P}, f, \boldsymbol{\xi}, Y, \boldsymbol{\Sigma}^p \} \,,$$

denotes the set of generalized forces conjugate to $\dot{\Lambda}$. Correspondingly, we assume that external agencies can drive power expenditure according to the equation

$$\mathcal{P}_{\text{ext}}(\mathcal{V}) = \int_{\partial P} \boldsymbol{t} \cdot \dot{\boldsymbol{\chi}} \, \mathrm{d}A + \int_B \boldsymbol{b} \cdot \dot{\boldsymbol{\chi}} \, \mathrm{d}V + \int_{\partial B} \zeta \dot{\phi} \, \mathrm{d}A \,, \tag{2.10}$$

where $\boldsymbol{t}$ is a surface traction, $\boldsymbol{b}$ is a body force, and ζ is a generalized surface traction that consumes power through the phase-field rate. The generalized velocities $\dot{\tilde{\varepsilon}}^p$ and $\dot{\boldsymbol{F}}^p$ are considered internal variables, which cannot be directly driven by external causes, and thus do not appear in the external power.

In order to apply the principle of virtual power, let us define admissible variations of the generalized velocities. Imagine that the generalized velocities are perturbed at any given fixed time t, in a manner consistent with the constraints (2.1), (2.2), (2.6) and such that the perturbation is null where there are prescribed Dirichlet boundary conditions. We write these spatial variations as

$$\tilde{\mathcal{V}} = \left\{ \widetilde{\boldsymbol{\chi}}, \widetilde{\phi}, \widetilde{\tilde{\varepsilon}^p}, \widetilde{\boldsymbol{F}^p} \right\}. \tag{2.11}$$

The principle of virtual power states that the actual generalized velocity fields $\mathcal{V}$ adopted by the system at time t are those such that

$$G(\mathcal{V}, \tilde{\mathcal{V}}) = 0, \qquad \text{for all admissible } \tilde{\mathcal{V}}; \tag{2.12}$$

where

$$G(\mathcal{V}, \tilde{\mathcal{V}}) = \int_{B_0} \left(\boldsymbol{P}(\mathcal{V}) : \boldsymbol{\nabla}\widetilde{\boldsymbol{\chi}} + \boldsymbol{\Sigma}^p(\mathcal{V}) : \widetilde{\boldsymbol{F}^p} + Y(\mathcal{V})\widetilde{\tilde{\varepsilon}^p} + f(\mathcal{V})\widetilde{\phi} + \boldsymbol{\xi}(\mathcal{V}) \cdot \boldsymbol{\nabla}\widetilde{\phi} \right) \mathrm{d}V - \mathcal{P}_{\text{ext}}(\tilde{\mathcal{V}}), \tag{2.13}$$

where we have indicated the possible functional dependence of the generalized forces on the velocities. (Note that the generalized forces also depend on $\mathcal{U}$, but these are considered fixed parameters at the given time t).

For the purpose of finite element discretization, the weak statement of the balance laws in the form of Equation (2.12) is all that is required. However, for completeness, we record the implied strong form:

$$\left.\begin{aligned} \boldsymbol{\nabla}\cdot\boldsymbol{P}+\boldsymbol{b}&=\boldsymbol{0}\\ -\boldsymbol{\nabla}\cdot\boldsymbol{\xi}+f&=0\\ (\boldsymbol{\Sigma}^p\boldsymbol{F}^{pT}):\boldsymbol{N}^p+Y&=0 \end{aligned}\right\} \quad \text{in } B_0 \tag{2.14}$$

$$\begin{aligned} \boldsymbol{P}\boldsymbol{n}&=\hat{\boldsymbol{t}} \quad \text{on } \partial_t B\\ \boldsymbol{\xi}\cdot\boldsymbol{n}&=\hat{\zeta} \quad \text{on } \partial_\zeta B \end{aligned} \tag{2.15}$$

Equation (2.14)a is recognized as the classical force balance for static equilibrium. Equation (2.14)b is an additional balance law imposed on the phase field; as we shall see, for typical choices of the constitutive relations, this balance law takes the form of an Allen-Cahn equation in which the damage field plays the role of the unconserved order parameter. The balance law (2.14)c represents the yield function. Note that (2.14)c contains no spatial derivatives and therefore is local in nature.

Equations (2.15) represent the natural boundary conditions. The boundary subsets appearing therein are subject to the standard restrictions

$$\begin{aligned} \partial_t B_0\cup\partial_{\boldsymbol{\chi}}B_0&=\partial B_0, & \partial_t B_0\cap\partial_{\boldsymbol{\chi}}B_0&=\emptyset\\ \partial_\zeta B_0\cup\partial_\phi B_0&=\partial B_0, & \partial_\zeta B_0\cap\partial_\phi B_0&=\emptyset \end{aligned}$$

If one can find a density function $w(\boldsymbol{\nabla}\boldsymbol{\chi},\dot{\phi},\boldsymbol{\nabla}\dot{\phi},\dot{\bar{\varepsilon}}^p,\dot{\boldsymbol{F}}^p)$ such that each of the generalized forces is equal to the partial derivative of w with respect to the conjugate generalized velocity, then the principle of virtual power (2.12) is the stationary point of the functional

$$I(\mathcal{V})=\int_{B_0} w(\boldsymbol{\nabla}\dot{\boldsymbol{\chi}},\dot{\phi},\boldsymbol{\nabla}\dot{\phi},\dot{\bar{\varepsilon}}^p,\dot{\boldsymbol{F}}^p)\,\mathrm{d}V-\mathcal{P}_{\text{ext}}(\mathcal{V}). \tag{2.16}$$

which furnishes the sought variational structure. Such a density function can be found by application of the method of variational constitutive updates [18].

Constitutive framework

To close the system, constitutive equations must be specified for each of the generalized forces in $\mathcal{F}$ and the flow direction $\boldsymbol{N}^p$. To proceed, we first deduce the restrictions the laws of thermodynamics and frame invariance place on the form of the constitutive equations.

Let ψ be the free energy density (per unit volume in the reference configuration). Under isothermal conditions, the first and second laws of thermodynamics reduce to the free energy imbalance

$$\mathcal{P}_{\text{ext}}(\mathcal{V}) - \int_P \dot{\psi}\, \mathrm{d}V \geq 0.$$

From the first law of thermodynamics, we have

$$\mathcal{P}_{\text{ext}}(\mathcal{V}) = \mathcal{P}_{\text{int}}(\mathcal{V}), \tag{2.17}$$

so we may write

$$\mathcal{P}_{\text{int}}(\mathcal{V}) - \int_P \dot{\psi}\, \mathrm{d}V \geq 0.$$

Since this inequality must hold for any arbitrary part P, this result may be localized to yield the dissipation inequality

$$\mathcal{D} = \boldsymbol{P} : \boldsymbol{\nabla}\dot{\boldsymbol{\chi}} + \boldsymbol{\Sigma}^p : \dot{\boldsymbol{F}}^p + Y\dot{\bar{\varepsilon}}^p + f\dot{\phi} + \boldsymbol{\xi} \cdot \boldsymbol{\nabla}\dot{\phi} - \dot{\psi} \geq 0. \tag{2.18}$$

Concomitant with our assumptions of power expenditure (cf. (2.8)), we assume that the local thermodynamic state depends on the degrees of freedom $\mathcal{U}$ through the set

$$\Lambda = \left\{ \boldsymbol{F}, \boldsymbol{F}^p, \bar{\varepsilon}^p, \phi, \boldsymbol{\nabla}\phi \right\}. \tag{2.19}$$

We consequently assume constitutive relations of the form

$$\begin{aligned} \psi &= \hat{\psi}(\Lambda); \quad \boldsymbol{P} = \hat{\boldsymbol{P}}(\Lambda); \\ \boldsymbol{\xi} &= \hat{\boldsymbol{\xi}}(\Lambda); \quad \boldsymbol{\Sigma}^p = \hat{\boldsymbol{\Sigma}}^p(\Lambda). \end{aligned} \tag{2.20}$$

As we wish to consider rate-dependence of plastic deformation and fracture in the theory, we assume that the generalized forces Y and f may be separated additively into equilibrium and non-equilibrium parts via

$$Y = Y^{\text{eq}}(\Lambda) + Y^{\text{neq}}(\dot{\bar{\varepsilon}}^p; \Lambda) \qquad\qquad f = f^{\text{eq}}(\Lambda) + f^{\text{neq}}(\dot{\phi}; \Lambda). \tag{2.21}$$

The equilibrium forces depend only on the current thermodynamic state, while the non-equilibrium forces depend on the conjugate rate variables. The constitutive relations for the non-equilibrium forces must vanish as their respective rates tend to zero.

The time derivative of the free energy function may be expanded to

$$\dot{\psi} = \frac{\partial\hat{\psi}(\Lambda)}{\partial \boldsymbol{F}} : \dot{\boldsymbol{F}} + \frac{\partial\hat{\psi}(\Lambda)}{\partial \boldsymbol{F}^p} : \dot{\boldsymbol{F}}^p + \frac{\partial\hat{\psi}(\Lambda)}{\partial\bar{\varepsilon}^p}\dot{\bar{\varepsilon}}^p + \frac{\partial\hat{\psi}(\Lambda)}{\partial\phi}\dot{\phi} + \frac{\partial\hat{\psi}(\Lambda)}{\partial\boldsymbol{\nabla}\phi} \cdot \boldsymbol{\nabla}\dot{\phi}. \tag{2.22}$$

Inserting this identity into the dissipation inequality (2.18) and applying the Coleman-Noll procedure leads to the conclusions

$$\begin{aligned} &\hat{\boldsymbol{P}}(\Lambda) = \frac{\partial\hat{\psi}(\Lambda)}{\partial \boldsymbol{F}}, \quad \hat{\boldsymbol{\Sigma}}^p(\Lambda) = \frac{\partial\hat{\psi}(\Lambda)}{\partial \boldsymbol{F}^p}, \qquad \hat{\boldsymbol{\xi}}(\Lambda) = \frac{\partial\hat{\psi}(\Lambda)}{\partial\boldsymbol{\nabla}\phi}, \\ &\hat{f}^{\text{eq}}(\Lambda) = \frac{\partial\hat{\psi}(\Lambda)}{\partial\phi}, \qquad\qquad \text{and} \qquad\qquad \hat{Y}^{\text{eq}}(\Lambda) = \frac{\partial\hat{\psi}(\Lambda)}{\partial\bar{\varepsilon}^p}. \end{aligned} \tag{2.23}$$

With these identities, the dissipation inequality reduces to

$$\mathcal{D} = Y^{\rm neq}(\dot{\bar{\varepsilon}}^p;\Lambda)\dot{\bar{\varepsilon}}^p + f^{\rm neq}(\dot{\phi};\Lambda)\dot{\phi} \geq 0. \tag{2.24}$$

As we wish to maintain a variational structure for the theory, we assume the existence of differentiable dual kinetic potentials $\Pi^*(\dot{\bar{\varepsilon}}^p;\Lambda)$ and $\Delta^*(\dot{\phi};\Lambda)$, which determine the non-equilibrium forces through

$$Y^{\rm neq}(\dot{\bar{\varepsilon}}^p,\Lambda) = \frac{\partial\Pi^*(\dot{\bar{\varepsilon}}^p;\Lambda)}{\partial\dot{\bar{\varepsilon}}^p}, \qquad\qquad f^{\rm neq}(\dot{\phi};\Lambda) = \frac{\partial\Delta^*(\dot{\phi};\Lambda)}{\partial\dot{\phi}}. \tag{2.25}$$

The material is assumed to be *strictly dissipative* in the sense of Gurtin et al. [7], namely,

$$\begin{cases} Y^{\rm neq}\,\dot{\bar{\varepsilon}}^p > 0, & \text{if } \dot{\bar{\varepsilon}}^p \neq 0; \\ f^{\rm neq}\,\dot{\phi} > 0, & \text{if } \dot{\phi} \neq 0. \end{cases} \tag{2.26}$$

Satisfaction of the dissipation inequality is then ensured if the each of the dual kinetic potentials obey the following conditions:

(C1) the dual kinetic potential is convex in its rate variable (for every Λ);

(C2) the dual kinetic potential achieves its minimum (for every Λ) when the rate variable is zero.

This may be demonstrated as follows. Convexity of Π^* means that

$$\Pi^*(\widetilde{\dot{\bar{\varepsilon}}}^p) \geq \Pi^*(\dot{\bar{\varepsilon}}^p) + \frac{\partial\Pi^*(\dot{\bar{\varepsilon}}^p)}{\partial\dot{\bar{\varepsilon}}^p}(\widetilde{\dot{\bar{\varepsilon}}}^p - \dot{\bar{\varepsilon}}^p),$$

for all nonnegative $\widetilde{\dot{\bar{\varepsilon}}}^p$ and $\dot{\bar{\varepsilon}}^p$. Let us take $\widetilde{\dot{\bar{\varepsilon}}}^p = 0$. Then by (C2), Π^* reaches the minimum value at $\widetilde{\dot{\bar{\varepsilon}}}^p$, which we denote by $\Pi^*_{\rm min}$, and we have

$$\frac{\partial\Pi^*(\dot{\bar{\varepsilon}}^p)}{\partial\dot{\bar{\varepsilon}}^p}\dot{\bar{\varepsilon}}^p \geq \Pi^*(\dot{\bar{\varepsilon}}^p) - \Pi^*_{\rm min}$$

or

$$Y^{\rm neq}\dot{\bar{\varepsilon}}^p \geq 0.$$

An identical proof holds for the dual kinetic potential $\Delta^*(\dot{\phi};\Lambda)$.

In the constitutive relation development we shall confine ourselves to dual kinetic potentials with properties (C1) and (C2), so that compliance with the dissipation inequality is guaranteed.

Specification of the constitutive relations

The free energy is partitioned into a mechanical part, which represents the stored energy of elastic and plastic work, and a fracture part, which represents the energy of creating new surface. The partition has the additive form

$$\hat{\psi} = \hat{\psi}_{\text{mech}}(\boldsymbol{F}, \boldsymbol{F}^p, \bar{\varepsilon}^p, \phi) + \hat{\psi}_{\text{frac}}(\phi, \boldsymbol{\nabla}\phi).$$

The dependence of the mechanical part on the phase field is included to allow the stress to relax as the damage increases. In particular, the mechanical free energy must vanish as $\phi \to 1$.

In the following two sections, we respectively specify the constitutive functions for the mechanical behavior and for the damage process.

Mechanical constitutive equations

It is convenient to first propose constitutive laws for the virgin material, as they take standard forms, and subsequently to augment them to account for the damage process. Let $\widetilde{\psi}$ be the free energy of the virgin material.[2] This energy is split into elastic and plastic parts as

$$\widetilde{\psi} = \widetilde{W}^e(\boldsymbol{F}^e) + \widetilde{W}^p(\bar{\varepsilon}^p), \tag{2.27}$$

where it is recalled that the elastic distortion is a derived quantity of the primitive variables $\boldsymbol{F}$ and $\boldsymbol{F}^p$ through $\boldsymbol{F}^e = \boldsymbol{F}\boldsymbol{F}^{p-1}$. Frame invariance requires that the elastic free energy depends on $\boldsymbol{F}^e$ only though $\boldsymbol{C}^e = \boldsymbol{F}^{eT}\boldsymbol{F}^e = \boldsymbol{F}^{p-T}\boldsymbol{C}\boldsymbol{F}^{p-1}$.

For $\widetilde{W}^e$ we choose the isotropic Hencky strain energy function

$$\widetilde{W}^e = \mu\boldsymbol{\varepsilon}^e : \boldsymbol{\varepsilon}^e + \frac{\lambda}{2}\operatorname{tr}(\boldsymbol{\varepsilon}^e), \tag{2.28}$$

where

$$\boldsymbol{\varepsilon}^e = \frac{1}{2}\log\big(\boldsymbol{F}^{eT}\boldsymbol{F}^e\big)$$

is the elastic Hencky strain (i.e., logarithmic strain), and $\mu > 0$ and $\lambda > 0$ are the elastic Lamé parameters. For the virgin plastic energy we choose Voce hardening, which is defined by the potential

$$\widetilde{W}^p = (A + \sigma_y)\,\bar{\varepsilon}^p + \frac{A}{n}\exp(-n\bar{\varepsilon}^p), \tag{2.29}$$

in which $\sigma_y > 0$ is the yield strength, $A > 0$ is the maximum increase in flow stress, and $n > 0$ is a dimensionless parameter that controls the rate of hardening with accumulated plastic strain.

[2] We shall follow the convention of placing a tilde over quantities associated with the virgin material.

The virgin material is taken to have power law rate sensitivity, defined by the dual kinetic potential

$$\widetilde{\Pi}^*(\dot{\bar{\varepsilon}}^p) = \frac{m\sigma_y\dot{\varepsilon}_0}{m+1}\left(\frac{\dot{\bar{\varepsilon}}^p}{\dot{\varepsilon}_0}\right)^{\frac{m+1}{m}}, \tag{2.30}$$

with $m > 0$ the rate sensitivity and $\dot{\varepsilon}_0 > 0$ a reference strain rate.

Next, we address the effect of damage on the mechanical constitutive behavior. Conceptually, damage is defined as a reduction of the capacity of the material to store energy. This process is represented by pre-multiplying the virgin material response with a *degradation function*, $g(\phi)\colon [0,1] \to [0,1]$ so that[3]

$$\hat{\psi}_{\text{mech}}(\boldsymbol{F}, \boldsymbol{F}^p, \bar{\varepsilon}^p, \phi) = g(\phi)\widetilde{\psi} = g(\phi)\left[\widetilde{W}^e(\boldsymbol{F}, \boldsymbol{F}^p) + \widetilde{W}^p(\bar{\varepsilon}^p)\right]. \tag{2.31}$$

In choosing this multiplicative form, we have retained the traditional form of continuum damage models, and in particular phase-field models of fracture [12, 1]. To be consistent with the notion of damage, the degradation function should be monotonically decreasing with the limits

$$g(0) = 1, \qquad\qquad g(1) = 0 \tag{2.32}$$

Thus, as the damage progresses from zero to one, the capacity of the material to store energy reduces and vanishes.

Just as the material loses elastic energy storage capacity with damage, it is reasonable to expect plastic dissipation to cease in damaged material points. We modify the virgin dual kinetic potential for plastic rate sensitivity in a similar fashion to obtain

$$\Pi^*(\dot{\bar{\varepsilon}}^p, \phi) = g(\phi)\widetilde{\Pi}^*(\dot{\bar{\varepsilon}}^p) \tag{2.33}$$

where $\widetilde{\Pi}^*(\dot{\bar{\varepsilon}}^p)$ is given in equation (2.33). It bears noting that the rate potential meets the conditions (C1) and (C2) specified above to ensure thermodynamic consistency.

From these constitutive relations we can derive the expressions for the generalized forces. Let $\boldsymbol{T}^e$ denote the stress conjugate to the elastic Hencky strain. For isotropic materials, it can be shown that $\boldsymbol{T}^e$ is equivalent to the stress measure [15, 9]

$$\boldsymbol{M} = \boldsymbol{F}^{eT}\boldsymbol{P}\boldsymbol{F}^{pT}, \tag{2.34}$$

which is sometimes referred to as the *Mandel stress*, a nomenclature we adopt. Evidently, the Mandel stress and the elastic Hencky strain are related through

$$\boldsymbol{M} = g(\phi)\left[2\mu\boldsymbol{\varepsilon}^e + \lambda\,\mathrm{tr}(\boldsymbol{\varepsilon}^e)\mathbf{1}\right]. \tag{2.35}$$

From equations (2.23) and (2.29) the equilibrium flow stress is given by

$$Y^{\text{eq}}(\bar{\varepsilon}^p) = g(\phi)\Big\{\sigma_y + A\big(1 - \exp(n\bar{\varepsilon}^p)\big)\Big\}$$

[3]The most common choice in the literature is $g(\phi) = (1-\phi)^2$. We examine this choice in the present report and identify several others we wish to investigate further in the future; see Table 2.1.

The constitutive equation for the rate sensitive, non-equilibrium part of the flow stress is

$$Y^{\text{neq}} = g(\phi)\left[\sigma_y \left(\frac{\dot{\bar{\varepsilon}}^p}{\dot{\varepsilon}_0}\right)^{1/m}\right].$$

Next we address the constitutive equation for $\boldsymbol{N}^p$. The flow direction is determined by appealing to the postulate of maximum dissipation. First, note that the constitutive function $\hat{\psi}(\boldsymbol{F}, \boldsymbol{F}^p, \bar{\varepsilon}^p, \phi)$ depends on $\boldsymbol{F}$ and $\boldsymbol{F}^p$ only through $\boldsymbol{F}^e = \boldsymbol{F}\boldsymbol{F}^{p-1}$. Using this we can derive the identities

$$\frac{\partial \hat{\psi}}{\partial \boldsymbol{F}^e} = \frac{\partial \psi}{\partial \boldsymbol{F}} \boldsymbol{F}^{pT} = \boldsymbol{P}\boldsymbol{F}^{pT} \tag{2.36}$$

$$\boldsymbol{\Sigma}^p = \frac{\partial \hat{\psi}}{\partial \boldsymbol{F}^p} = -\boldsymbol{F}^{eT}\frac{\partial \psi}{\partial \boldsymbol{F}} = -\boldsymbol{F}^{eT}\boldsymbol{P} \tag{2.37}$$

The dissipation due to plastic flow is given by $Y^{\text{neq}}\dot{\bar{\varepsilon}}^p$. Using the balance law (2.14)c, one finds

$$\begin{aligned} Y^{\text{neq}} &= -(\boldsymbol{\Sigma}^p \boldsymbol{F}^{pT}) : \boldsymbol{N}^p - Y^{\text{eq}} \\ &= (\boldsymbol{F}^{eT}\boldsymbol{P}\boldsymbol{F}^{pT}) : \boldsymbol{N}^p - Y^{\text{eq}} \end{aligned}$$

and therefore the plastic dissipation due to plastic flow may be written

$$\left[\boldsymbol{M} : \boldsymbol{N}^p - Y^{\text{eq}}\right]\dot{\bar{\varepsilon}}^p$$

where we have used the definition of the Mandel stress (2.34). Since $\dot{\bar{\varepsilon}}^p \geq 0$, dissipation is clearly maximized if $\boldsymbol{N}^p$ has the same direction as $\boldsymbol{M}$. Using this fact and enforcing the constraints (2.2) gives

$$\boldsymbol{N}^p = \sqrt{\frac{3}{2}}\frac{\operatorname{dev}(\boldsymbol{M})}{\|\operatorname{dev}(\boldsymbol{M})\|}. \tag{2.38}$$

where the operator $\operatorname{dev}(\cdot)$ takes the deviatoric part of its argument. Equation (2.38) is the sought constitutive relation for the flow direction tensor.

With these constitutive relation choices in place, the balance law (2.14)c—i.e., the yield equation—can be written in the familiar form

$$\bar{\sigma} - Y = 0$$

where we have defined the *effective stress*

$$\begin{aligned} \bar{\sigma} &= \boldsymbol{M} : \boldsymbol{N}^p \\ &= \sqrt{(3/2)}\|\operatorname{dev}\boldsymbol{M}\|, \end{aligned}$$

which is the finite deformation counterpart of the Mises equivalent stress from classical small-strain J_2 plasticity theory.

Fracture constitutive equations

The fracture energy is taken to have the form

$$\psi_{\text{frac}}(\phi, \boldsymbol{\nabla}\phi) = \frac{G_c}{4\ell c_h}\Big(h(\phi) + \ell^2 \|\boldsymbol{\nabla}\phi\|^2\Big) \tag{2.39}$$

The function $h(\phi) : [0,1] \to \mathbb{R}$, which we refer to as the *damage potential*, controls the local part of the energy spent in the fracture process. The gradient term in (2.39) is responsible for regularization, preventing spurious localization of the damage into vanishingly small bands as the mesh is refined. The parameter $\ell > 0$ (dimensions of length) controls the length scale over which crack is smeared, while the parameter $G_c > 0$ (dimensions of energy per unit area) represents the critical energy release rate of the material. The pre-factor c_h is given by

$$c_h = \int_0^1 \sqrt{h(\phi)}\, \mathrm{d}\phi\,,$$

and is introduced to ensure that the fracture energy per unit area predicted by the model comes out as G_c; it is not an adjustable parameter.

Rate sensitivity is introduced into the damage evolution as a numerical technique for regularizing problems with unstable crack growth. For this purpose, simple linear kinetics suffices. Hence we use the dual kinetic potential

$$\Delta^*(\dot{\phi}) = \frac{\eta}{2}\dot{\phi}^2, \tag{2.40}$$

where $\eta > 0$ is a rate constant with dimensions of energy $\times$ time $\times$ length^{-3}.

The generalized forces conjugate to the phase field follow from the Coleman-Noll relations (2.23) and the constitutive equations (2.39) and (2.40) as

$$f^{\text{eq}} = g'(\phi)\left(\widetilde{W}^e + \widetilde{W}^p\right) + h'(\phi) \tag{2.41}$$

$$f^{\text{neq}} = \eta\dot{\phi} \tag{2.42}$$

From Equations (2.23) and (2.39) the constitutive equation for the force conjugate to $\boldsymbol{\nabla}\phi$ is

$$\boldsymbol{\xi} = \frac{G_c\ell}{4c_h}\boldsymbol{\nabla}\phi. \tag{2.43}$$

Substituting the chosen constitutive equations into the balance law (2.14)b yields

$$\eta\dot{\phi} = \frac{G_c\ell}{4c_h}\nabla^2\phi - \frac{\partial}{\partial\phi}\left(\psi_{\text{mech}}(\boldsymbol{F}, \boldsymbol{F}^p, \bar{\varepsilon}^p, \phi) + \frac{G_c\ell}{4c_h}h(\phi)\right), \tag{2.44}$$

which is an Allen-Cahn equation for ϕ. However, unlike typical applications of the Allen-Cahn equation which use a double-well potential, the local free energy density in the present case (the term in parentheses) has only a single minimum.

Particular phase field models are specified by choices of the dimensionless functions $g(\phi)$ and $h(\phi)$. Several options have appeared in the literature; we have implemented the first two in Table 2.1. Both models are compared later in this report. Note that the Tupek and Lorentz models introduce additional adjustable parameters (ψ_{crit} in both models, and additionally p in the Lorentz model). These additional parameters grant them a richer representation of fracture physics that include not just a fracture energy, but also a critical strength. This grants them an interpretation as regularizations of *cohesive models* of fracture. These models are not investigated further in this report, but will be examined in future work.

Table 2.1: Some phase-field models and their degradation functions and damage potentials.

Model	$g(\phi)$	$h(\phi)$	c_h
Classical	$(1-\phi)^2$	ϕ^2	$1/2$
Threshold	$(1-\phi)^2$	ϕ	$2/3$
Lorentz	$\dfrac{(1-\phi)^2}{(1-\phi)^2 + \frac{3}{8}\frac{G_c/\ell}{\psi_{\text{crit}}}(1+p\phi)}$	ϕ	$2/3$
Tupek	$\dfrac{1-\phi}{1+(\frac{3}{8}\frac{G_c/\ell}{\psi_{\text{crit}}}-1)\phi}$	ϕ	$2/3$

Chapter 3

Implementation

Overview

The ductile failure models using a phase-field approach described in Chapter 2 are implemented into *Sierra/SM* as a material model within *Sierra*'s *Library of Advanced Materials for Engineering* (*LAMÉ*) [20]: *PhaseFieldFeFp*. This class contains the initialization and stress calculation methods that *Sierra/SM* calls to determine the material state at every integration point. Several aspects of the implementation are discussed in this section.

Instead of the damage field ϕ, the implementation is phrased in terms of its complement $c = 1 - \phi$. We refer to this field as the *coherence*. Both conventions are used in the literature; as this represents a simple substitution, the equations that define the phase-field model are only slightly changed when posed in terms of coherence.

Phase field update

In the *Sierra/SM* phase-field implementation, the implicit phase-field solves are performed using a reaction-diffusion solver that predated this effort. The solver is evaluated at nodes within element blocks specified in the input files, and solves scalar reaction-diffusion partial differential equations of the form:

$$Rc - D\nabla^2 c = S \tag{3.1}$$

where R indicates the reaction coefficient, D indicates the diffusion coefficient, and S indicates the source term. The coefficients derive from the substitution of specific degradation functions and damage potentials (presented in Table 2.1) into Equation (2.44) and are presented in Table 3.1, where $\epsilon \ll 1$ represents a small conditioning coefficient and where we have defined the quantity $\psi_{\text{crit}} = 3G_c/(16\ell)$ for convenience. In *Sierra/SM*, these coefficients R, D, S are further scaled by inverse cube of the length scale $1/\ell^3$ to maintain a predictable system conditioning.

Table 3.1: Coefficients of reaction-diffusion solver for implicit phase-field update.

Model	R	D	S
Classical	$\left(\frac{4\ell\psi_{\text{mech}}(1-\epsilon)}{G_c}+1\right)$	$4\ell^2$	1
Threshold	$\left(\frac{\langle\psi_{\text{mech}}-\psi_{\text{crit}}\rangle}{\psi_{\text{crit}}}(1-\epsilon)+1\right)$	$4\ell^2$	1

As noted in Chapter 1, there are constraints on the coherence field that should be considered in the implementation. The constraint $c \geq 0$ is naturally satisfied by the models considered in this report, in the sense that the fracture driving force defined in the models vanishes in the limit $c \to 0$. This is demonstrated in Chapter 4 in the context of a homogeneous deformation, where it is seen that the coherence approaches zero asymptotically. Thus, this constraint need not be externally imposed, at least in quasi-statics or implicit dynamics simulations. The constraint $1 \geq c$ is automatically satisfied by the Classical model, but the not by the Threshold model (as the name implies, damage begins upon attainment of a critical condition). This constraint is handled in an approximate manner introduced by Miehe et al. [17], wherein Macaulay brackets are introduced in the reaction term to ensure that damage grows only after the energetic threshold ψ_{crit} is reached.

When using explicit dynamics, the satisfaction of the phase bound constraints can no longer be guaranteed through the form of the driving forces, and additional precautions must be taken.[1] In the implementation, the phase field is bounded as $0 \leq c \leq 1$ within the explicit integration operator such that phase values that exceed the bounds after the time step update are immediately reset to the corresponding bound before proceeding to the next time step.

The final type of constraint, damage irreversibility, is not explicitly accounted for in this *Sierra/SM* implementation of the phase-field models. Thus, in the current state, this capability should only be used for *monotonic* loading. We will address this in future work.

Time integration

Several temporal integration schemes have been implemented in the *Sierra/SM* phase-field capability:

- Implicit mechanical solution, implicit phase-field solution ("implicit/implicit")

[1] This is a typical feature of applying explicit time integration in the presence of unilateral constraints, as the driving forces are defined from the *previous* time step, and there is no global iteration to ensure that the external and internal driving forces at the updated time step are in balance. This behavior is also seen, for example, with contact.

- Explicit mechanical solution, implicit phase-field solution ("explicit/implicit")
- Explicit mechanical solution, explicit phase-field solution ("explicit/explicit")

The initial implementation employs the *Sierra/SM* reaction-diffusion equation solver to perform the phase-field update, making the phase-field solution implicit. This pairs especially well with the implicit time integration of the mechanical solution that allows analysts to take large timesteps to complete the simulation efficiently. In each timestep, the mechanical update is performed, followed by the phase-field update – a staggered solution scheme for the coupled system (see Figure 3.1). This integration has been performed with the phase rate constant η set to zero. It is conceptually convenient to think of η as a phase viscosity.

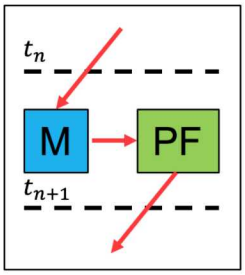

Figure 3.1: Diagram showing the staggered solution scheme that performs the mechanical (M) then phase-field (PF) solves in sequence within each timestep.

However, many *Sierra/SM* users prefer to use explicit time integration, a choice driven by the model size as well as higher reliability and support for explicit analysis in *Sierra/SM*, especially for large models with contact. This motivates the inclusion of explicit time integration as a solution option. The explicit/implicit option represents the usage of explicit time integration for the mechanics combined with the reaction-diffusion solve for the phase field every timestep. This approach works, but is quite expensive; the explicit mechanical solution requires a great many timesteps that are each relatively inexpensive to compute; in contrast, the reaction-diffusion solve requires the solution of a matrix system, which is relatively costly. This combines to an approach with very many timesteps that are each relatively time-consuming. In an effort to reduce this expense, the reaction-diffusion solver does have an user-input option to reduce the frequency of the phase-field solve.

Another option to reduce computation time when using explicit time integration is to use an explicit phase-field solution as well. Our implementation follows the approach of Tupek [22] which employs a non-zero phase rate constant $\eta > 0$ to regularize the the problem. This term allows the phase balance law (2.44) to be solved explicitly:

$$\eta \frac{(\phi_{n+1} - \phi_n)}{\Delta t_n} = C\nabla^2 \phi_n - \frac{\partial}{\partial \phi}\big(\psi_{\text{mech}}(\boldsymbol{F}_n, \boldsymbol{F}^p{}_n, \bar{\varepsilon}^p_n, \phi_n) + h(\phi_n)\big), \tag{3.2}$$

$$\phi_{n+1} = \phi_n + \frac{\Delta t_n}{\eta}\left(C\nabla^2\phi_n - \frac{\partial}{\partial\phi}\big(\psi_{\text{mech}}(\boldsymbol{F}_n, \boldsymbol{F^p}_n, \bar{\varepsilon}^p_n, \phi_n) + h(\phi_n)\big)\right). \tag{3.3}$$

This enables the explicit/explicit approach to proceed using the critical timestep from the mechanical solve and without requiring a matrix phase-field solve at each timestep. This approach is implemented and available as part of the *PhaseFieldFeFp* model in *Sierra/SM*.

Chapter 4

Numerical Examples

Local behavior in homogeneous deformations

Some light can be shed onto the phase-field models in Table 2.1 by examining their behavior in the simple case of uniaxial tension. Being a homogeneous deformation, the gradients of all fields vanish, and consequently the balance law for the phase (2.14)b reduces to

$$f = 0.$$

To attain additional simplicity, we suppress the rate sensitivity of the phase kinetics, so that the balance law simplifies even further to

$$f^{\text{eq}} = g'(\phi)\widetilde{\psi} + h'(\phi) = 0.$$

This is a *local* equation that may be solved explicitly for ϕ as a function of the applied stretch and internal variables.

Taking each phase-field model in turn, we substitute the constitutive equation for $\widetilde{\psi}_{\text{mech}}$ and the appropriate constitutive equations for $g(\phi)$, $h(\phi)$. In the case of the classical phase-field model, we arrive at

$$\text{(classical)} \qquad \phi = \frac{\widetilde{\psi}}{\widetilde{\psi} + \frac{G_c}{2\ell}}. \tag{4.1}$$

Effecting the same for the threshold model gives

$$\text{(threshold)} \qquad \phi = 1 - \frac{\psi_{\text{crit}}}{\widetilde{\psi}}, \tag{4.2}$$

where we again refer to the quantity $\psi_{\text{crit}} = 3G_c/(16\ell)$ for convenience. In order to respect the phase bounds (2.4), Eq. (4.2) is only valid for $\widetilde{\psi} \geq \psi_{\text{crit}}$, demonstrating the physical significance of ψ_{crit} as an energetic threshold for damage growth. This inequality is reflected in the implementation by the use of Macaulay brackets in the reaction term (refer to Table 3.1). Note that in both models, the parameters G_c and ℓ only appear together in the ratio G_c/ℓ for homogeneous deformations, which we consider here as a single material parameter.

Under the present focus of isotropic material behavior, the deformation gradient at each step is necessarily diagonal. Assuming that the imposed uniaxial deformation is in the X_1

direction, the deformation gradient has the form $\boldsymbol{F} = \mathrm{diag}(\lambda, \lambda_{\mathrm{lat}}, \lambda_{\mathrm{lat}})$, where λ_{lat} is the lateral Poisson stretch required to maintain the stress-free conditions in the X_2 and X_3 directions. The uniaxial loading condition can be imposed simply by a simulation with a single hexahedral element.

The direct normal component of the Mandel stress in the direction of loading is given by $M_{11} = (1-\phi)^2 E\varepsilon^e$, while all other components vanish. Any other desired stress tensor for output can be obtained by the appropriate transformation. We will use the *Kirchhoff* stress for output as it is equal to the Mandel stress in uniaxial loading and is conjugate to the logarithmic strain.[1] In uniaxial tension, the logarithmic strain, the elastic logarithmic strain, and the Kirchhoff stress are related in exactly the same way as the strain, plastic strain, and Cauchy stress in the classical small-strain J_2 flow theory.

First, let us consider the case of phase-field models applied to a virgin material model that is purely elastic. The material modulus is taken to be $E = 200\,\mathrm{MPa}$. The elastic logarithmic strain appearing in the stress-strain relation reduces to the total logarithmic strain $\varepsilon = \log\lambda$, and the axial Kirchhoff stress is given by

$$\tau = (1-\phi)^2 E\varepsilon. \tag{4.3}$$

For the classical model, we choose three values of G_c/ℓ and plot the response in Figure 4.2. The virgin material stress-strain relationship is shown in a broken line for comparison. Increasing G_c/ℓ raises the peak stress attained; thus, as expected from fracture mechanics, increasing the toughness or reducing the fracture process zone size increases the local strength. The peak stress τ_c can be expressed analytically by finding the critical point of (4.3); the result of this calculation is

$$\frac{G_c}{\ell} = \frac{256}{27}\frac{\tau_c^2}{E}.$$

The values of G_c/ℓ used to make Figure 4.2 are such that peak stress is 400 MPa, 500 MPa, and 600 MPa. From Figure 4.1b, it is seen that the phase field begins to grow immediately. This is an essential feature of the classical model. By substituting in the expression in (4.1) for the phase into the stress-strain relation (4.3), it is seen that the stress goes as ε^{-1} at large strains. This results in a rather gradual decay, as is evident in Figure (4.1a).

Next, we turn our attention to the threshold model. As the name implies, damage does not initiate immediately, but rather requires the attainment of a critical condition. Recall that the phase field is subject to the constraint $\phi \geq 0$. Thus Eq. (4.2) determines the phase field only when $\widetilde{\psi}(\boldsymbol{F}, \bar{\varepsilon}^p) \geq \psi_{\mathrm{crit}}$; otherwise, the constraint is active and the damage is held fixed at zero. The response of the threshold model is illustrated in Figure 4.2. For ease of comparison, we have chosen values of G_c/ℓ such that peak stresses are approximately equal

[1] In general, the Kirchhoff stress is conjugate to the spatial logarithmic strain; in the special case of null rotation (as in uniaxial tension), the referential and spatial logarithmic strains coincide and it is not necessary to distinguish between them.

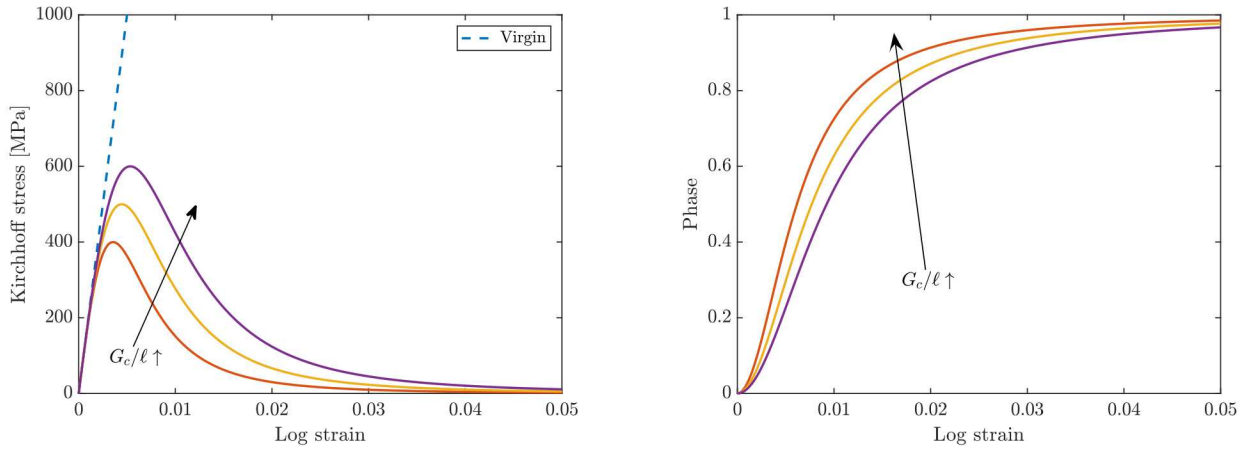

Figure 4.1: Behavior of classical phase-field model in uniaxial tension with an elastic constitutive model. (a) Stress-strain response. (b) Evolution of phase (i.e., damage) with strain.

to the classical model example (400 MPa, 500 MPa, and 600 MPa). The peak stress is attained at the point of damage initiation. For uniaxial tension, this point is

$$\frac{\tau_c^2}{2E} = \psi_{\text{crit}} = \frac{3}{16} G_c/\ell$$

Substituting in (4.2) for the phase in the stress-strain relation (4.3) reveals that the stress goes as ε^{-3} once the threshold is met. Thus the damage decays significantly faster than the classical model, which is evident when comparing Figures 4.1a and 4.2a (note the scales of the strain axes are not equal).

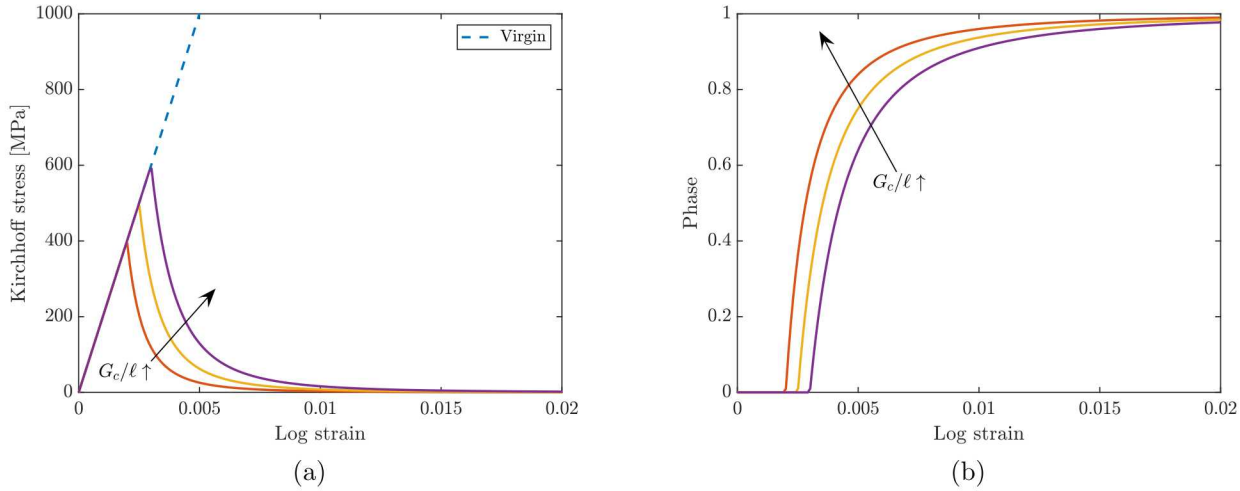

Figure 4.2: Behavior of threshold phase-field model in uniaxial tension with an elastic constitutive model. (a) Stress-strain response. (b) Evolution of phase (i.e., damage) with strain. The thresholding of the phase evolution inherent to this model is apparent.

We examine elastic-plastic virgin material behavior next. In order to simplify the comparison to its essence, we suppress plastic rate sensitivity (in addition to the suppression of phase field kinetics as above). The parameters of the Voce hardening model are set to approach simple linear hardening. The specific values of the elastic-plastic material properties given in Table 4.1.

Table 4.1: Material model parameters for uniaxial material point simulation.

E	σ_y	A	n
200 GPa	400 MPa	40 GPa	0.01

For the classical model, we select the values $G_c/\ell = \{1 \times 10^3, 2.5 \times 10^3, 10 \times 10^3\} \times \sigma_y^2/E$. The response is plotted in Figure 4.3. It is evident that damage significantly affects the stress-strain behavior at even small strains close to yield strain. This is contrary to expectations for metal plasticity, where experience shows that plastic deformation due to dislocation glide is well described by plasticity model alone. Any damage process should intervene rather suddenly near final failure point. Very large values of G_c/ℓ are needed to even approach the virgin, undamaged response at modest strains. For a given G_c, this requires small values of ℓ to get reasonable behavior, which in turns requires finer spatial discretization. The slow unloading of the classical model (also observed in the elastic case) is also problematic. In opposition to the demand for large G_c/ℓ to obtain reasonable material behavior, the slow decay of the stress with strain is exacerbated by increasing G_c/ℓ. These contrary requirements are difficult to balance. For example, although the largest chosen value of G_c/ℓ is only able to provide reasonable elastic-plastic behavior at strains of at most a few percent, the stress remains significant at a log strain of 3 (which corresponds to a stretch of 20!). One can conjecture that in non-homogeneous deformations, appreciable damage is likely to occur even in regions remote from crack tips unless very small length scales are used.

The threshold model is examined next with elastic-plastic behavior. The values of G_c/ℓ are chosen such that damage initiates at approximately $\varepsilon = \{0.1, 0.2, 0.3\}$.[2] This computation is made by assuming that the elastic energy is negligible in comparison to the plastic work, and thus G_c/ℓ can be estimated as $\psi_{\text{crit}} \approx \sigma_y \bar{\varepsilon}^p + 0.5 H_0 \bar{\varepsilon}^{p2}$. The undamaged elastic-plastic behavior is preserved until the threshold is crossed. As a consequence, the plasticity parameters can be characterized in an conventional manner from tension tests, uncoupled from the damage evolution. The stress decay in the damage phase still goes as ε^{-3} as in the elastic case, and unloading occurs much more rapidly than in the classical model. For these reasons, the threshold model is recommended over the classical model for elastic-plastic problems.

Due to the thresholding behavior, damage can be isolated to the desired crack regions in non-homogeneous deformations by setting ℓ small enough. In some problems, this can be accomplished with reasonable values of ℓ; we will demonstrate an example in a later section. However, by analogy with cohesive zone modeling of ductile fracture, we anticipate that

[2]For comparison with the classical model, this corresponds to $G_c/\ell \approx \{280, 590, 920\} \times \sigma_y^2/E$.

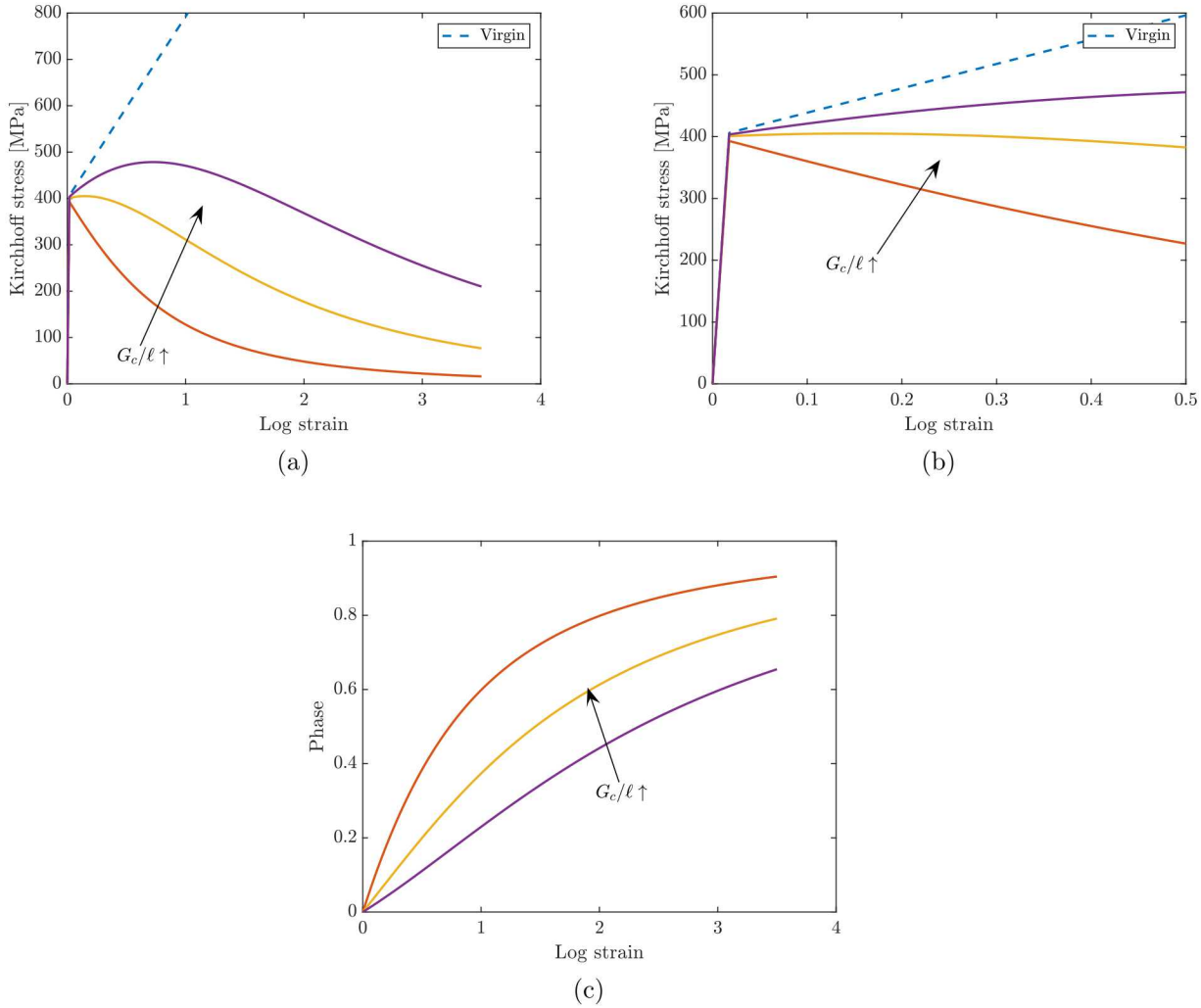

Figure 4.3: Behavior of classical phase-field model in uniaxial tension. (a) Stress-strain response. Note very large strains are required for stress to decay (b) Same stress-strain response, view restricted to smaller strain. (c) Evolution of phase (i.e., damage) with strain.

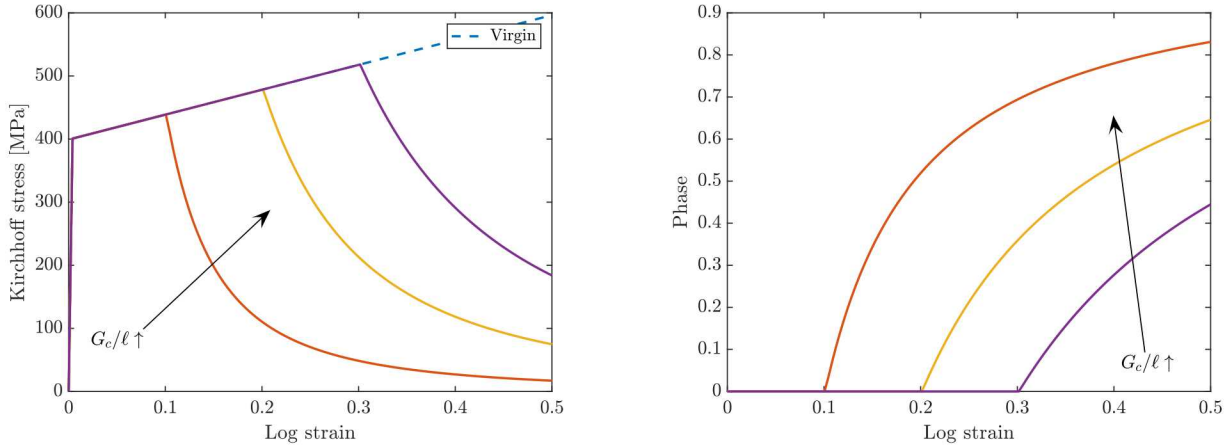

(a) (b)

Figure 4.4: Behavior of threshold phase-field model in uniaxial tension with an elastic-plastic constitutive model. (a) Stress-strain response. (b) Evolution of phase (i.e., damage) with strain.

independent characterization of the peak strength, the fracture energy, and the unloading curve shape may prove useful in some large-scale yielding problems. Such concerns motivate the use of cohesive zone-type phase field models [13, 14], which we endeavor to examine in future work.

Demonstration problem: compact tension specimen

In order to more rigorously test this phase-field models implemented, we developed a series of tests based on the ASTM compact tension specimen [10] made of 6061-T6 aluminum. These tests evaluate the model performance over all three time integration techniques discussed in Chapter 3: implicit mechanics/implicit phase-field, explicit mechanics/implicit phase-field, and explicit mechanics/explicit phase-field with viscous regularization.

The specimen geometry was developed according to ASTM standard E1820-17a at the smallest allowable thickness $b/w = 4$ for computational efficiency. Also to reduce simulation time, symmetry is employed to reduce the simulation domain to one-quarter the original, cutting the domain horizontally through the notch and through the thickness as shown in Figure 4.5. One version of the mesh was developed with a sharp crack tip, and another was developed with a rounded crack tip. These meshes are presented in Figure 4.6 and 4.7, respectively. The geometric parameters are provided in Table 4.2.

To avoid having to consider contact, the loading pins are modeled as half-circles meshed in the pin-holes and fully connected to the compact tension specimen. Free rotation around

Table 4.2: Compact tension specimen geometric parameters.

Parameter	Variable	USCS Value	Unit	SI Value	Unit
specimen width	w	4.0	in	101.6	mm
specimen thickness	b	1.0	in	25.4	mm
pin radius	r	0.5	in	12.7	mm
initial crack-length/width ratio	a_0/w	$[0.2, 0.5]$	-	$[0.2, 0.5]$	-

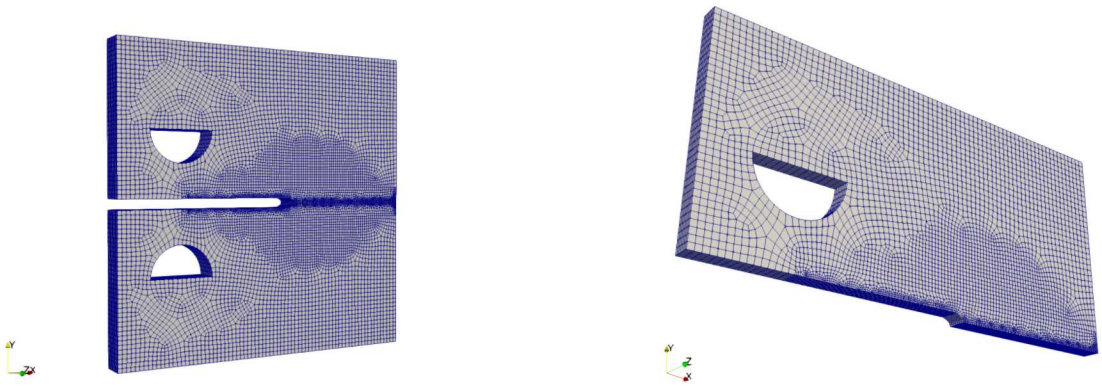

(a) Full mesh (b) Symmetry model

Figure 4.5: Mesh of compact tension specimen.

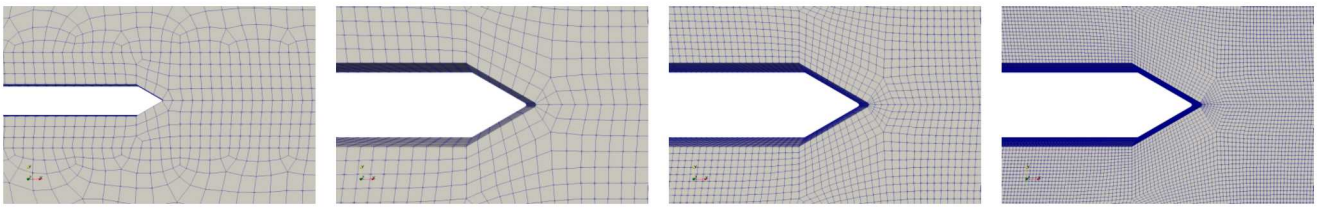

(a) 20 elem./in. (b) 40 elem./in. (c) 80 elem./in. (d) 160 elem./in.

Figure 4.6: Compact tension specimen symmetry model with sharp crack tip.

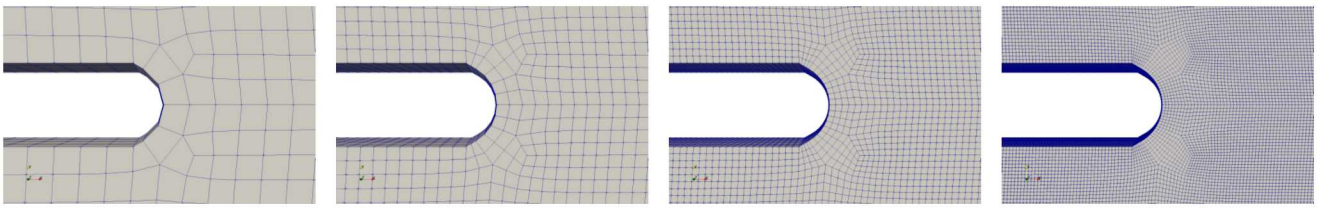

(a) 20 elem./in. (b) 40 elem./in. (c) 80 elem./in. (d) 160 elem./in.

Figure 4.7: Compact tension specimen symmetry model with rounded crack tip.

the pin is approximated by applying vertical displacements only along a nodeset at the pin centroid. This permits the pin material to rotate around the nodeset. These boundary conditions are not perfect, but decently approximate the loading conditions in a computationally inexpensive way. The pin material is set to be artificially strong (yield stress $\sigma_y = 10^{30}$ Pa) such that it does not develop damage. In dynamics, the density is scaled by 10^6 to ensure that the pin does not control the critical timestep, though this may have implications for the dynamic response of the specimen – the validity of this choice will be further explored in the future. Unless otherwise mentioned, the specimen material being modeled in these test simulations is aluminum 6061-T6. The material parameters were fit from a calibration to the plasticity model described in Chapter 2, implemented in *Sierra/SM* as the *LAMÉ* material model *FeFp*. The aluminum was fit to a Voce hardening model with the flow stress $\bar{\sigma}$ defined as [20]:

$$\bar{\sigma}(\bar{\varepsilon}^p) = \sigma_y + A\left(1 - \exp(-n\bar{\varepsilon}^p)\right). \tag{4.4}$$

The material and model parameters for this are presented in Table 4.3.

Table 4.3: Compact tension specimen material and model parameters.

Parameter	Variable	USCS Value	Unit	SI Value	Unit
density	ρ	0.0975	lbf/in^3	2700	kg/m^3
Young's modulus	E	10000	ksi	69	GPa
Poisson's ratio	ν	0.33	-	0.33	-
fracture toughness	K_{IC}	26.4	ksi-in$^{1/2}$	29	MPa-m$^{1/2}$
toughness	G_c	69.6	lbf/in	12188	J/m^2
yield strength	σ_y	40.35	ksi	278.2	MPa
Voce hardening modulus	A	8.868	ksi	61.14	MPa
Voce hardening exponent	n	26.34	-	26.34	-
length scale	ℓ	0.0667	in	1.693	mm
conditioning coefficient	ϵ	10^{-4}	-	10^{-4}	-

Implicit Integration

The first capability demonstrated with the compact tension specimen is crack nucleation and propagation across the entire specimen in an artificially ductile material. The coherence c and plastic strain $\bar{\varepsilon}^p$ fields are presented Figures 4.8 & 4.9. A threshold of $c \geq 0.5$ is used in these visualizations to give the appearance of an opening crack. This is necessary as the phase field fully damages the material ($\phi = 1$, $c = 0$) very rarely, but yet a fracture localization certainly exists. Albeit subjective, a visual threshold provides the discontinuity expected

from a fracture model. From Figure 4.9, it is evident that the plasticity has localized to a narrower band than the fracture length scale.

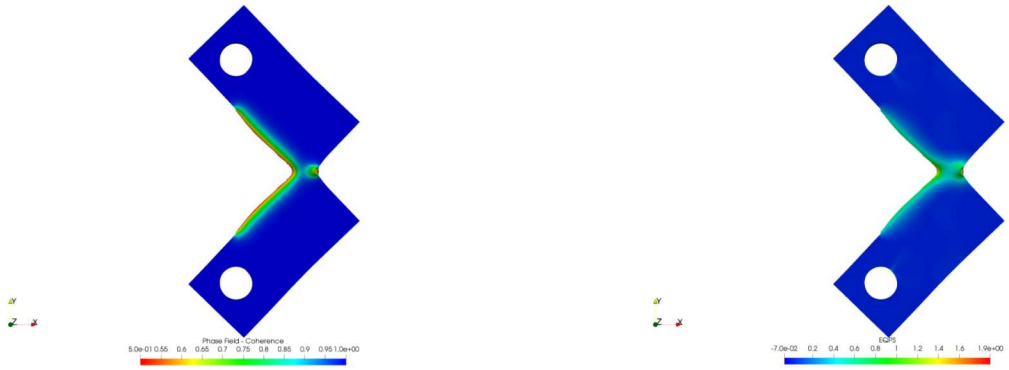

(a) c (b) $\bar{\varepsilon}^p$

Figure 4.8: Symmetry model of a compact tension specimen using the classical phase-field model using a rounded-tip mesh showing deformed results with a visual threshold at $c \geq 0.5$ ($\phi \leq 0.5$).

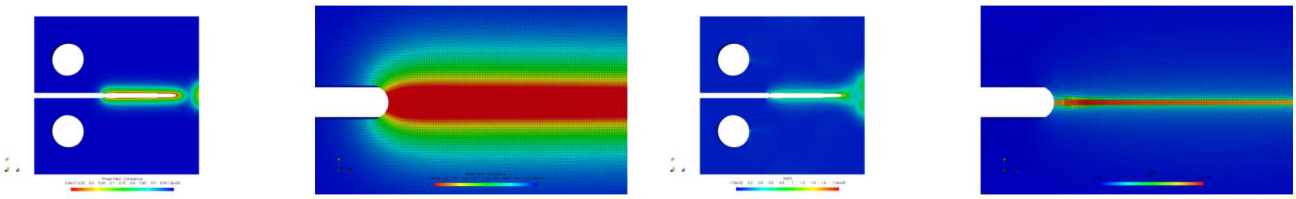

(a) c (b) c (close-up) (c) $\bar{\varepsilon}^p$ (d) $\bar{\varepsilon}^p$ (close-up)

Figure 4.9: Symmetry model of a compact tension specimen using the classical phase-field model using a rounded-tip mesh showing undeformed results with and without a visual threshold at $c \geq 0.5$ ($\phi \leq 0.5$).

Mesh convergence

Using the same artificial material, the mesh is refined from 20 elements per inch to 40 and 80 elements per inch. This is presented in Figure 4.10 and demonstrates clear convergence of the force/displacement history. The fracture energy (2.39) converges but at a slow rate as the crack propagates.

Toughness test / temporal convergence

Next, in an effort to verify whether the crack is nucleating at the expected force, the classical and threshold models are each evaluated using the 6061-T6 aluminum material properties. In this exercise, the peak applied force is interpreted as corresponding to the crack

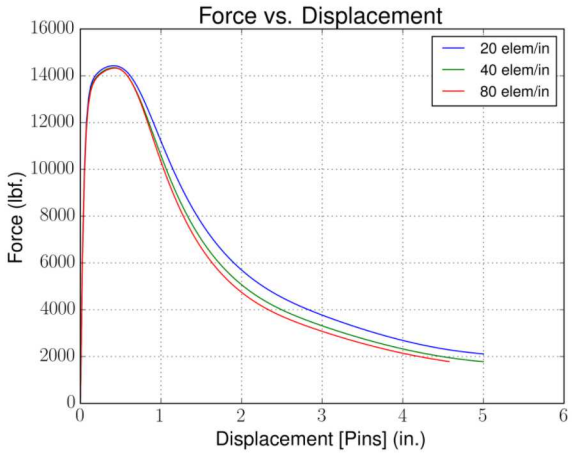

(a) Force/Displacement

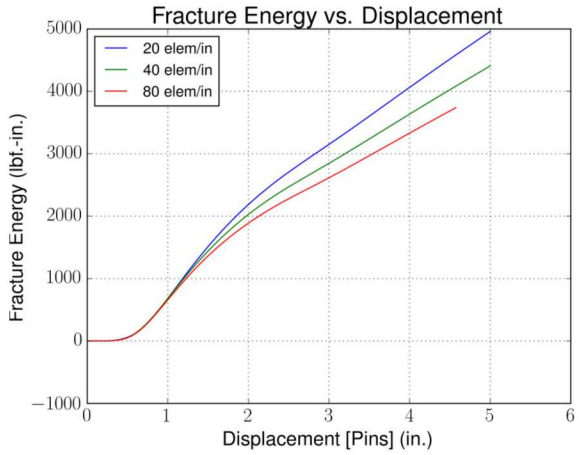

(b) Fracture Energy

Figure 4.10: Mesh convergence study of compact tension specimen with $a_0/w = 0.3$ using rounded-tip meshes and a fixed timestep with the classical phase-field model.

driving force just overcoming the resistance to extend the crack further into the material. This peak force is compared to the expected force as can be estimated from the ASTM E1820-17a's stress intensity factor relation for the compact tension specimen: Equations (A2.2) & (A2.4) [10]. This stress intensity factor estimate is reproduced here:

$$K = \frac{P}{b\sqrt{w}} f(a/w), \tag{4.5}$$

$$f(x) = \frac{(2+x)\left(0.886 + 4.64x - 13.32x^2 + 14.72x^3 - 5.6x^4\right)}{(1-x)^{3/2}}. \tag{4.6}$$

A similar estimate can be found in the Stress Analysis of Cracks Handbook [21]. This relation can be inverted to yield the critical force at which crack propagation occurs:

$$P_{cr} = \frac{K_{IC} b\sqrt{w}}{f(a_0/w)}. \tag{4.7}$$

Substituting the geometric and material parameters from Tables 4.2 & 4.3 yields $P_{cr} =$ 24.4 kN. The classical and threshold models were evaluated at a variety of timesteps for this toughness test, with the base timestep set as $\Delta t = 1.0$ ms and refined thrice by half. These results are presented in Figures 4.11 & 4.12, respectively. Both models tend toward a critical force for crack propagation very near to the analytical prediction (4.7).

The results appear to be temporally convergent, but nonetheless reveal a strong sensitivity to the timestep. As this problem employs implicit time integration, the base timestep of $\Delta t = 1.0$ ms was prescribed, rather than deriving from a physical characteristic. This

sensitivity means that an analyst would be prudent to consider the role of the selected timestep when using implicit integration. The source of this sensitivity was further explored by considering a "local" phase-field model (i.e. disabling the gradient term, $C = 0$). We conclude that this sensitivity stems from the usage of the staggered integration scheme of the coupled system, as discussed in Chapter 3, and believe that if the mechanical and phase-field solves were to iterate within the timestep, that this sensitivity would be greatly reduced. This follows the "alternate minimization" technique described by Bourdin *et al.* [4] and now common to the phase-field community. Another possibility is to solve the coupled system simultaneously, though this does not seem to be widely performed.

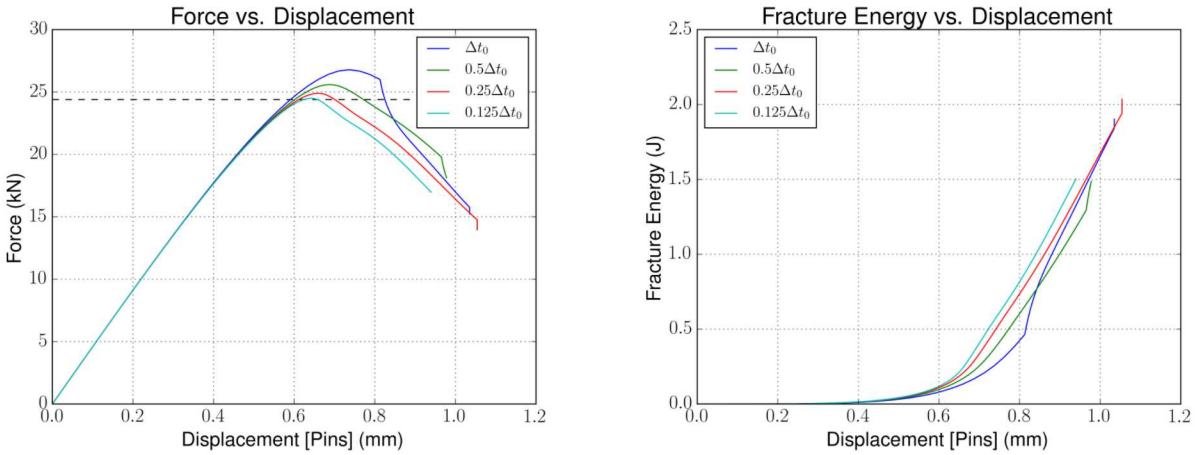

(a) Force/Displacement (b) Fracture Energy

Figure 4.11: Temporal convergence study of compact tension specimen with $a_0/w = 0.5$ using the 40 elem./in. sharp-tip mesh with the classical phase-field model. The analytical prediction of critical force for crack propagation is plotted as a dashed black line.

Mixed Integration

The next case tested is mixed time integration, that is explicit time integration for the mechanical system and implicit time integration for the phase evolution system. For this case, the timestep is governed by the critical timestep of the conventional mechanical system. Each timestep, the mechanical system is integrated explicitly. At a frequency selected by the user, the phase-field updates via implicit reaction-diffusion solve after the mechanics. As discussed in Chapter 3, this might result in a fantastically slow simulation, as the implicit solve is quite expensive and might be called very often. A potential method of time savings, therefore, is to update the phase-field less often than the mechanical system. This case compared the results between updating the phase field every timestep against updating it every two, four, eight, 10, 100, or 1000 timesteps.

This was evaluated on the aluminum compact tension specimen described above, using an

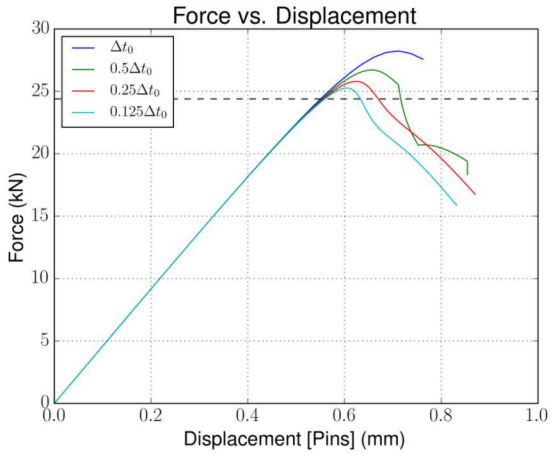

(a) Force/Displacement

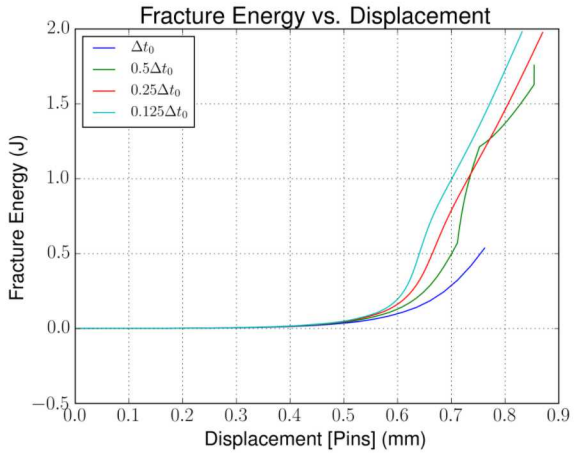

(b) Fracture Energy

Figure 4.12: Temporal convergence study of compact tension specimen with $a_0/w = 0.5$ using the 40 elem./in. sharp-tip mesh with the threshold phase-field model. The analytical prediction of critical force for crack propagation is plotted as a dashed black line.

additional mass scaling factor of 10 on the aluminum's density. These results are presented in Figure 4.13. The timing study presented in Figure 4.13c demonstrates the time savings realized in this problem by altering the phase-field solve frequency. For this problem, the approaches only visiblly diverge between the 10 and 100 frequencies, indicating that great time savings may be realized at negligible accuracy loss. It is worth noting that the explicit timestep for this problem is approximately 55 ns, so increasing the phase-field solve frequency to every 550 ns or 5.5 μs is still far below the implicit timesteps explored in the previous section.

Explicit Integration

The final case evaluated is explicit time integration for both the mechanical and phase-field updates. The explicit phase-field update (3.3) takes advantage of the phase viscosity term (2.40) by using a non-zero phase viscosity parameter η. The stability of the temporal integration depends on the phase viscosity parameter chosen and can be determined by identifying the highest derivative terms of Equation (2.44), $\dot{\phi}$ and $\nabla^2\phi$, and replacing them with differential terms: $1/\Delta t_{PF}$ and $1/(\Delta x)^2$.

$$\eta \frac{1}{\Delta t_{PF}} \geq C \frac{1}{(\Delta x)^2} \tag{4.8}$$

This creates an estimate for the stable timestep Δt_{PF} of the parabolic phase-field update partial differential equation. It is convenient to have the explicit timestep calculated by *Sierra/SM* for the mechanical system Δt_M be the smallest timestep, so that it governs the

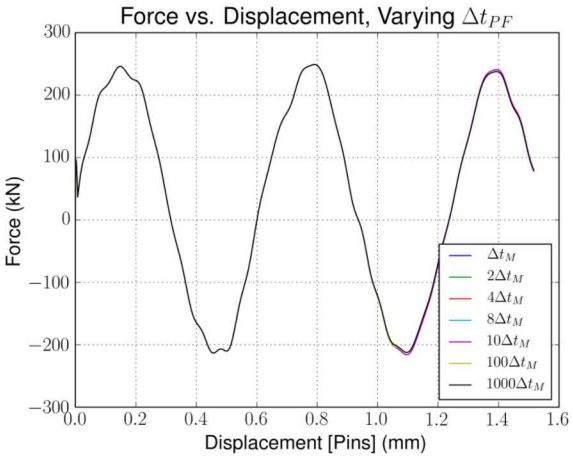

(a) Force/Displacement

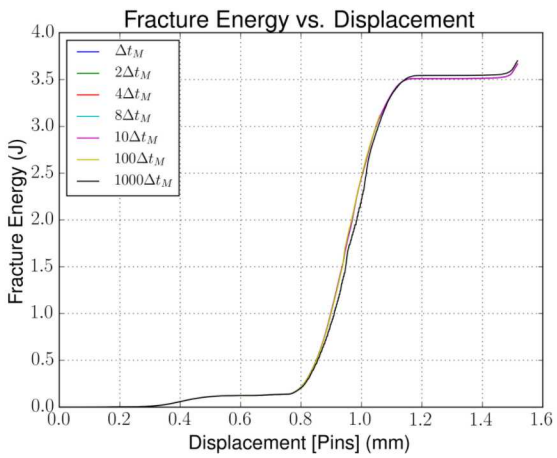

(b) Fracture Energy

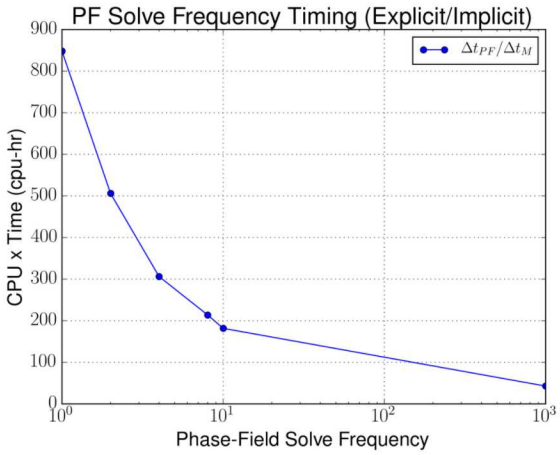

(c) Timing Study

Figure 4.13: Phase-field solve frequency study of compact tension specimen with $a_0/w = 0.5$ using the 20 elem./in. sharp-tip mesh with the explicit/implicit classical phase-field model.

system stability:

$$\Delta t_M \leq \Delta t_{PF} \leq \frac{\eta}{C}(\Delta x)^2. \tag{4.9}$$

Inverting this relation gives an estimate for the minimum value of the phase viscosity parameter that ensures stability of the phase field update. Recognizing that the critical mechanical timestep Δt_M relates to the minimum length scale Δx and the solid wave speed v_c, the minimum viscosity can be written in terms of those quantities:

$$\eta \geq \left(\frac{C\Delta t_M}{(\Delta x)^2} = \frac{C}{v_c \Delta x} \right) \tag{4.10}$$

As the partial differential equation governing the phase field update is parabolic, the critical viscosity value does depend on the mesh size Δx. This may detract from the mesh convergence of the explicit time integration scheme, as the simulation may be unstable with a constant parameter value and refined mesh or might be non-convergent with a changing parameter value. The rate-dependence and dissipative effects that this viscosity parameter have yet to be quantified.

Considering the scaled system in the reaction-diffusion template form that has been implemented, D/ℓ^3 replaces C as the gradient-term coefficient.

$$\eta \geq \left(\frac{D}{\ell^3 v_c \Delta x} = \frac{4}{\ell \sqrt{E/\rho} \Delta x} \right) \tag{4.11}$$

Substituting the material properties presented in Table 4.3 and mass scaling of 10 yields a critical viscosity value of $\eta \geq 14806$ s/m^3. To provide a margin of safety, a value of $\eta = 30000$ s/m^3 has been selected for this example.

The explicit/explicit results at two different levels of phase viscosity η are presented and compared to an explicit/implicit result for the classical and threshold phase-field models in Figures 4.14 & 4.15, respectively. Additionally, an explicit/explicit result with a non-increasing timestep is also considered. The result show a close agreement between the two integration methods for both phase-field models. The responses diverge only slightly for the higher viscosity parameter. These results show that the implemented explicit/explicit integration scheme is a promising option going forward. More testing is needed to quantify the mesh convergence of this method and further explore the sensitivity to the phase viscous parameter η.

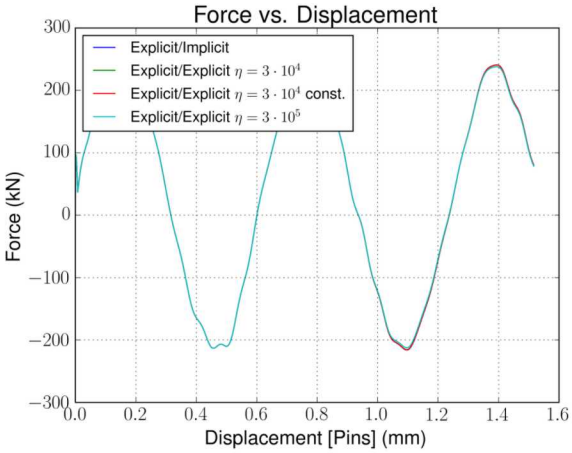

(a) Force/Displacement

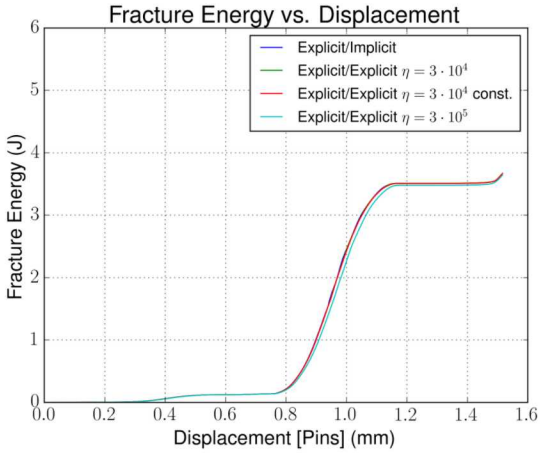

(b) Fracture Energy

Figure 4.14: Phase viscosity study of compact tension specimen with $a_0/w = 0.5$ using the 20 elem./in. sharp-tip mesh with the classical phase-field model.

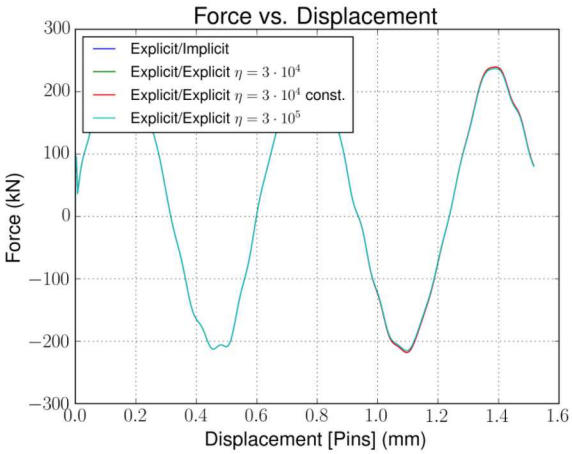

(a) Force/Displacement

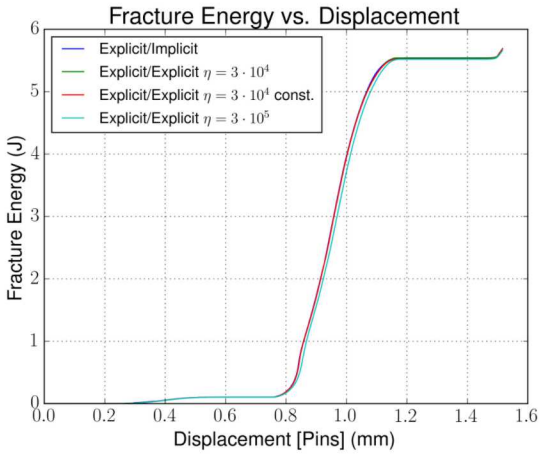

(b) Fracture Energy

Figure 4.15: Phase viscosity study of compact tension specimen with $a_0/w = 0.5$ using the 20 elem./in. sharp-tip mesh with the threshold phase-field model.

Chapter 5

Discussion

Summary of work done

In the 2018 fiscal year, we began by conducting a literature review on regularized models for ductile failure that exist in the scientific literature. A promising and very active approach is the phase-field method for fracture, a continuum model that diffuses damage in the neighborhood of a crack according to a length-scale parameter. This approach derives from an energy functional in which the Griffith-type surface energy terms are approximated by a volumetric term that is a function of the damage gradient and the length scale.

We implemented the phase-field model for fracture into *Sierra/SM* using a reaction-diffusion solver and a hyperelastic plasticity model. Two distinct phase-field models are included in this implementation: the classical model and the threshold model. Using this phase-field implementation, we developed single-element tests to verify the model response in elastic (brittle) and elastic-plastic (ductile) materials. The model was then applied to a compact tension specimen, a common mode-I fracture problem with overwhelmingly tensile fields, to further evaluate the model behavior. With a tensile loading, the phase-field model successfully localized and propagated damage in the expected fracture field. Mesh convergence and temporal convergence of the models were confirmed using the compact tension specimen. The apparent toughness of the compact tension specimen, as measured by the maximum force required to propagate a crack, was convergent to the material toughness given as a simulation input.

Our subsequent efforts were to extend the implicit time integration of the phase field evolution to explicit time integration. First, a mixed integration scheme was developed in which the mechanical system is integrated explicitly and the phase field is updated implicitly. It was found that performing the phase field update less frequently than the explicit time integration greatly reduced the runtime at minimal cost of simulation quality. Then, the phase-field models were extended to fully explicit time integration by employing a viscous regularization of the phase-field update. We briefly discussed the estimation of a stable regularization parameter and found that the explicitly integrated results compared well to the mixed-integration results.

Outlook and future work

We believe that the phase-field fracture model is poised to be an effective and robust failure model that can be used for Sandia's production-level analysis of abnormal mechanical environments. At this point, there are many opportunities of this work to improve the capability and credibility of the phase field models implemented. These include:

- Timing study of the explicit time integration compared to mixed time integration
- Mesh refinement study of explicitly integrated model, with a focus on evaluating any consequences of the viscous regularization
- Toughness verification using explicit time integration, perhaps using a simplified geometry with specific boundary conditions applied into order to eliminate dynamic effects
- Revising the coupling of the mechanical and phase field solves to iterate within the staggered solution, commonly referred to as "alternate minimization" in the phase-field community [4]
- Assessment of phase-field model on representative problems from Sandia weapons systems groups
- Extension of the phase-field update to handle the solution nonlinear partial differential equations, to allow implementation of a cohesive phase field model
- Intelligent consideration of phase-field constraints such as damage bounding and irreversibility
- Modularization of the phase-field models so that they can be coupled with any material model implemented in *Sierra/SM*

This group looks forward to addressing these points in the 2019 fiscal year.

References

[1] Roberto Alessi, Marreddy Ambati, Tymofiy Gerasimov, Stefano Vidoli, and Laura De Lorenzis. Comparison of phase-field models of fracture coupled with plasticity. In *Advances in Computational Plasticity*, pages 1–21. Springer, 2018.

[2] Roberto Alessi, Jean-Jacques Marigo, and Stefano Vidoli. Gradient damage models coupled with plasticity and nucleation of cohesive cracks. *Archive for Rational Mechanics and Analysis*, 214(2):575–615, 2014.

[3] Marreddy Ambati, Tymofiy Gerasimov, and Laura De Lorenzis. Phase-field modeling of ductile fracture. *Computational Mechanics*, 55(5):1017–1040, 2015.

[4] Blaise Bourdin, Gilles A. Francfort, and Jean-Jacques Marigo. Numerical experiments in revisited brittle fracture. *Journal of the Mechanics and Physics of Solids*, 48(4):797–826, 2000.

[5] Blaise Bourdin and Jean-Jacques Francfort, Gilles A .and Marigo. The variational approach to fracture. *Journal of Elasticity*, 91(1-3):5–148, 2008.

[6] Gilles A. Francfort and Jean-Jacques Marigo. Revisiting brittle fracture as an energy minimization problem. *Journal of the Mechanics and Physics of Solids*, 46(8):1319–1342, 1998.

[7] Morton E. Gurtin, Eliot Fried, and Lallit Anand. *The Mechanics and Thermodynamics of Continua*. Cambridge University Press.

[8] Vincent Hakim and Alain Karma. Laws of crack motion and phase-field models of fracture. *Journal of the Mechanics and Physics of Solids*, 57(2):342–368, 2009.

[9] Anne Hoger. The stress conjugate to logarithmic strain. *International Journal of Solids and Structures*, 23(12):1645–1656, 1987.

[10] ASTM International. Standard test method for measurement of fracture toughness. Technical standard E1820-17a, ASTM International, West Conshohocken, PA, 2017.

[11] Milan Jirásek. Nonlocal models for damage and fracture: comparison of approaches. *International Journal of Solids and Structures*, 35(31-32):4133–4145, 1998.

[12] Jean Lemaitre. A continuous damage mechanics model for ductile fracture. *Journal of Engineering Materials and Technology*, 107(1):83–89, 1985.

[13] Eric Lorentz, Sam Cuvilliez, and Kyrylo Kazymyrenko. Convergence of a gradient damage model toward a cohesive zone model. *Comptes Rendus Mécanique*, 339(1):20–26, 2011.

[14] Eric Lorentz, Sam Cuvilliez, and Kyrylo Kazymyrenko. Modelling large crack propagation: from gradient damage to cohesive zone models. *International Journal of Fracture*, 178(1-2):85–95, 2012.

[15] Jean Mandel. Equations constitutives et directeurs dans les milieux plastiques et viscoplastiques. *International Journal of Solids and Structures*, 9(6):725–740, 1973.

[16] Christian Miehe, Fadi Aldakheel, and Arun Raina. Phase field modeling of ductile fracture at finite strains: A variational gradient-extended plasticity-damage theory. *International Journal of Plasticity*, 84:1–32, 2016.

[17] Christian Miehe, Martina Hofacker, and Fabian Welschinger. A phase field model for rate-independent crack propagation: Robust algorithmic implementation based on operator splits. *Computer Methods in Applied Mechanics and Engineering*, 199(45-48):2765–2778, November 2010.

[18] Michael Ortiz and Laurent Stainier. The variational formulation of viscoplastic constitutive updates. *Computer Methods in Applied Mechanics and Engineering*, 171(3-4):419–444, 1999.

[19] R.H.J. Peerlings, R. De Borst, W.A.M. Brekelmans, and J.H.P. De Vree. Gradient enhanced damage for quasi-brittle materials. *International Journal for Numerical Methods in Engineering*, 39(19):3391–3403, 1996.

[20] William M. Scherzinger and Brian T. Lester. Library of Advanced Materials for Engineering (LAMÉ) 4.48. SAND Report SAND2018-3231, Sandia National Laboratories, Albuquerque, NM and Livermore, CA, 2018.

[21] Hiroshi Tada, Paul C. Paris, and George R. Irwin. The Stress Analysis of Cracks Handbook. Technical report, Del Research Corporation, 1973.

[22] Michael R. Tupek. Cohesive phase-field fracture and a PDE constrained optimization approach to fracture inverse problems. SAND Report SAND2016-9510, Sandia National Laboratories, Albuquerque, NM and Livermore, CA, 2016.

[23] Clemens V. Verhoosel and René de Borst. A phase-field model for cohesive fracture. *International Journal for numerical methods in Engineering*, 96(1):43–62, 2013.

DISTRIBUTION:

1	MS 9042	Arthur Brown, 8752
1	MS 9042	Jay Dike, 8752
1	MS 0840	Brian Lester, 1554
1	MS 9042	Scott Peterson, 8343
1	MS 0840	William Scherzinger, 1554
1	MS 0845	Jesse Thomas, 1542
1	MS 0845	Michael Tupek, 1542
1	MS 0899	Technical Library, 8944 (electronic copy)


Sandia National Laboratories